

Effect of inorganic material surface chemistry on structures and fracture behaviours of epoxy resin

Received: 9 July 2023

Accepted: 15 February 2024

Published online: 08 March 2024

Check for updates

Tomohiro Miyata ¹, Yohei K. Sato¹, Yoshiaki Kawagoe ² ✉, Keiichi Shirasu ³ ✉, Hsiao-Fang Wang ⁴, Akemi Kumagai¹, Sora Kinoshita⁵, Masashi Mizukami ⁶, Kaname Yoshida ⁷, Hsin-Hui Huang⁷, Tomonaga Okabe ^{2,8,9}, Katsumi Hagita ¹⁰, Teruyasu Mizoguchi ¹¹ & Hiroshi Jinnai ¹ ✉

The mechanisms underlying the influence of the surface chemistry of inorganic materials on polymer structures and fracture behaviours near adhesive interfaces are not fully understood. This study demonstrates the first clear and direct evidence that molecular surface segregation and cross-linking of epoxy resin are driven by intermolecular forces at the inorganic surfaces alone, which can be linked directly to adhesive failure mechanisms. We prepare adhesive interfaces between epoxy resin and silicon substrates with varying surface chemistries (OH and H terminations) with a smoothness below 1 nm, which have different adhesive strengths by ~13 %. The epoxy resins within sub-nanometre distance from the surfaces with different chemistries exhibit distinct amine-to-epoxy ratios, cross-linked network structures, and adhesion energies. The OH- and H-terminated interfaces exhibit cohesive failure and interfacial delamination, respectively. The substrate surface chemistry impacts the cross-linked structures of the epoxy resins within several nanometres of the interfaces and the adsorption structures of molecules at the interfaces, which result in different fracture behaviours and adhesive strengths.

Over the past few decades, the development of materials and products that promote energy conservation has become increasingly important for achieving a sustainable society. Within the transportation industry, including aircraft, marine vessels, and automobiles, the substitution of inorganic materials with polymeric materials has been actively promoted to achieve weight reduction and improved energy efficiency^{1,2}. For instance, epoxy resin adhesives have replaced metal rivets and bolts in joining applications. Additionally, fibre-reinforced plastic, a composite comprising epoxy resin as the matrix and glass/carbon fibres as fillers, has been utilized in vehicle body panels for several decades. Epoxy resin is a crucial polymeric material in industrial applications owing to its exceptional thermal and adhesive properties and excellent workability¹⁻³.

Although epoxy-resin-based materials are energy-efficient alternatives to metals, they have a higher risk of mechanical failure. Major failure modes include delamination at the epoxy resin-inorganic material interfaces, which has long been recognized as a critical limitation of such composites⁴⁻⁷. Therefore, gaining a comprehensive understanding of the adhesion mechanisms and delamination/fracture behaviours occurring at the adhesive interfaces between epoxy resins and inorganic materials is desirable for effectively controlling the properties of epoxy resin-based adhesives and composites and improving their performance in a wide range of practical applications.

Adhesion mechanisms typically comprise two factors⁸: (i) chemical interactions, which involve chemical bonds such as covalent and

A full list of affiliations appears at the end of the paper. ✉ e-mail: kawagoe@tohoku.ac.jp; keiichi.shirasu.c1@tohoku.ac.jp; hiroshi.jinnai.d4@tohoku.ac.jp

hydrogen bonds, as well as van der Waals interactions between the materials in contact; and (ii) mechanical interactions that occur through the interlocking of two materials. Additionally, the interfacial regions play a critical role in the fracture behaviour as these areas can have weaker mechanical performance than the bulk materials^{9,10}. The relationship between epoxy resin structures and their fracture behaviour near adhesive interfaces is of considerable interest in the development of adhesive systems resistant to interfacial fracture and delamination¹¹.

Several studies have investigated the adhesive interfaces between epoxy resins and inorganic materials, aiming to elucidate the characteristics of the interfacial regions. X-ray reflectivity and scanning force microscopy-based force modulation microscopy have revealed that epoxy resins near an adhesive interface demonstrate confinement and higher stiffness than the bulk regions^{12,13}. The thicknesses of the interfacial regions vary from tens of nanometres to 1 μm , depending on the specific materials and measurement techniques used. Additionally, it has been observed that the amine-to-epoxy (stoichiometric) ratio differs in the interfacial regions compared to the bulk^{13,14}.

The surface chemistry of inorganic substrates is recognized as a significant factor affecting the adhesive strengths of epoxy resins^{2,11,15,16}. Furthermore, molecular dynamics (MD) simulations of curing reactions have shown that the surface chemistry can alter the cross-linked network structures of epoxy resin near adhesive interfaces¹⁷. However, the relationship between the surface chemistry and the cross-linked structures of epoxy resins near experimental adhesive interfaces remains unexplored. To obtain insights into this relationship, analytical techniques with a spatial resolution higher than the sizes of epoxy-resin monomers are necessary because the curing of epoxy resins involves interactions between epoxy resin molecules and inorganic surfaces.

Transmission electron microscopy (TEM) and scanning TEM (STEM) are powerful tools for observing atomic and molecular structures within materials at high resolution. Furthermore, STEM-based electron energy-loss spectroscopy (STEM-EELS) enables the examination of the spatial distributions of elements and chemical bonding states in materials. In 2022, STEM-EELS was used to investigate the rough interfaces between epoxy resins and aluminium substrates, but the spatial resolution (<5 nm) was insufficient to elucidate the effects of the surface chemistry on the cross-linked structures of epoxy resins near the adhesive interfaces¹⁸. Furthermore, the use of rough aluminium surfaces resulted in both chemical and mechanical interactions contributing to adhesion. This made it impossible to determine the individual effects of surface chemistry and surface roughness on the adhesion mechanisms. To comprehensively understand the effects of surface chemistry in isolation, it is necessary to conduct sub-nanometre-resolution observations of nearly atomically flat interfaces with various surface chemistries. Moreover, it is crucial to identify fracture paths with high resolution to establish a correlation between the epoxy resin structures and the fracture mechanisms near the adhesive interfaces.

In this study, we prepared planar adhesive interfaces between epoxy resin and silicon substrates with two different surface chemistries: hydroxyl and hydrogen terminations. To investigate these interfaces, we employed three techniques with molecular-scale resolutions: (i) STEM-EELS measurements, (ii) curing MD simulations, and (iii) fracture TEM observations. By integrating these techniques, we were able to provide new insights into the chemical compositions, cross-linked structures, and fracture surfaces near the adhesive interfaces. Finally, we explored the adhesion and fracture mechanisms that influence adhesive strength, which exclusively stem from chemical interactions and nanoscale molecular structures near the adhesive interfaces, thereby excluding mechanical interactions.

Results and discussion

Adhesive strengths between epoxy resin and Si substrates

We prepared adhesive interfaces between epoxy resin and Si substrates with OH- and H-terminated surfaces. Hereafter, we refer to these interfaces as the OH- and H-terminated interfaces. The epoxy resin used in this study was a mixture of bisphenol A diglycidyl ether (DGEBA) and 4,4-diaminodicyclohexylmethane (PACM). The chemical structures of DGEBA and PACM are depicted in Fig. 1. Lap-shear tests were conducted to measure the adhesive strengths of the OH- and H-terminated interfaces, yielding values of 34.8 ± 1.2 and 30.8 ± 1.8 MPa, respectively. These results indicate that the OH-terminated interface exhibits a higher average adhesive strength than the H-terminated interface. The surfaces of the Si substrates were characterized by a high level of flatness, with an arithmetic mean roughness of <0.5 nm determined using atomic force microscopy (AFM). Therefore, the adhesion between the epoxy resin and Si substrates is majorly governed by chemical interactions rather than mechanical interactions resulting from surface roughness. Essentially, the variation in adhesive strengths mainly stems from discrepancies in the surface chemistry of the Si substrates. The subsequent sections describe nanoscopic analyses of the adhesive interfaces to clarify the impact of the surface chemistry of the Si substrate on the cross-linked structures and fracture mechanisms of the epoxy resin close to these interfaces.

Electron microscopy images of the adhesive interfaces

Figure 2 presents annular dark-field STEM (ADF-STEM) images of the OH- and H-terminated interfaces observed along the <110> direction of the Si substrates, which correspond to single Si crystals. The columns of Si atoms are observed as bright spots (upper portions of Fig. 2a, b). Specifically, the OH- and H-terminated interfaces align with the {111} crystal planes. The epoxy resin layers in the lower regions of the images appear darker due to the presence of lighter elements (H, C, N, and O). At both the OH- and H-terminated interfaces, silicon oxide (SiO₂) layers with ~2 nm thickness were observed between the Si crystal and epoxy resin. The native oxide layers on the Si substrates were not removed during the surface treatment with dilute hydrofluoric (HF) acid (1.5 wt.%) and water-plasma treatments used to achieve the OH and H terminations. This was further supported by the thickness measurements of the oxide layer using ellipsometry (Supplementary Table 1). The characterization of the Si surfaces confirmed the presence of OH and H terminations achieved through the HF acid and water-plasma treatments, respectively. This was determined through water contact angle measurements and ATR-FTIR spectra, as shown in the Supplementary Information (Supplementary Figs. 1 and 3). Additionally, ellipsometry measurements (Supplementary Table 1) and ADF-STEM cross-sectional observations (Fig. 2) revealed that the natural oxide layer of the Si substrate remained intact after the HF acid treatment due to the significantly diluted (1.5 wt.%) nature of the HF acid solution.

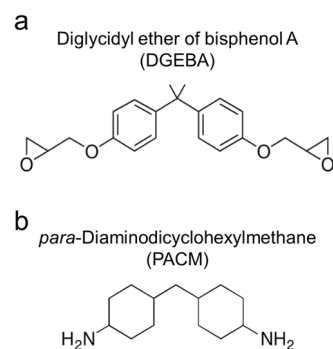


Fig. 1 | Molecular structures of the components of the epoxy resin. a DGEBA and **b** PACM.

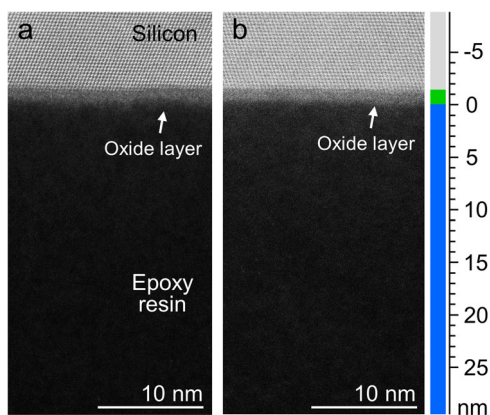


Fig. 2 | Cross-sectional annular dark-field scanning transmission electron microscopy (ADF-STEM) images of the adhesive interfaces. a OH-terminated and **b** H-terminated interfaces. Silicon oxide (SiO_2) layers are observed in both images. Source data are provided as Source Data files.

Consequently, the oxide layers on the Si substrates with different surface chemistries exhibited similar thicknesses. This facilitated a comparative analysis focused on the influence of surface chemistry on the interphase structure and fracture behaviour, with minimal consideration of surface morphology.

Surface chemistry of the Si substrates with epoxy resin

The surface chemistry of the Si substrates after pasting and curing the epoxy resin was analysed using STEM-EELS. Figure 3 shows the electron energy-loss near-edge structure (ELNES) spectra of the $\text{Si-L}_{2,3}$ absorption edges at the OH- and H-terminated interfaces. These spectra were precisely measured at the interfaces between the epoxy resin and 1 nm-wide oxide layers, as shown on the left side of Fig. 3a. The red and blue spectra correspond to the OH- and H-terminated interfaces, respectively. The spectrum of the OH-terminated interface resembles that of SiO_2 , with peaks observed at 106, 108, and 115 eV (as indicated by the vertical red lines and triangles in Fig. 3a). These characteristic peak positions indicate a chemical bonding state of Si atoms at the OH-terminated interface similar to SiO_2 , with the Si atoms adopting a tetrahedral arrangement, surrounded by four O atoms^{19–22}. In the spectrum of the H-terminated interface, the peaks at 106 and 108 eV are shifted towards lower energy by 0.3 eV compared to the spectrum of the OH-terminated interface.

To investigate the origin of the peak shifts, surface models were prepared with Si-OH and Si-H bonds, representing the OH and H terminations, respectively. An α -quartz (0001) dense surface was used as the model for the SiO_2 layers (Fig. 3b). Figure 3c displays the simulated $\text{Si-L}_{2,3}$ edge spectra for the Si atoms on the uppermost surface of these surface models. The black spectrum corresponds to the Si atoms on the surface of the α -quartz (0001) dense surface, with no groups other than Si-O-Si bonds. The red and blue spectra were simulated for the Si atoms in Si-OH and Si-H bonds, respectively. These simulated spectra reveal that the first peak in the spectrum of the Si atoms with a Si-H bond (H termination) exhibited a chemical shift towards the lower-energy side by 0.3 eV compared to that of the unmodified SiO_2 model. Conversely, the first peak shifted towards the higher-energy side by 0.5 eV for the Si atoms with a Si-OH bond (OH termination). These chemical shifts in the Si-H and Si-OH bonds resulted from the increased and decreased charges of the Si atoms, respectively, compared to the Si-O-Si termination.

In the STEM-EELS experiments, simultaneous measurements were performed on Si atoms inside the oxide layers and on their surfaces. Consequently, the spectra of the Si-H/Si-OH bonds on the surfaces overlapped with those of the oxide layers (SiO_2 bulk region). This explains why the experimentally observed spectra resemble that of

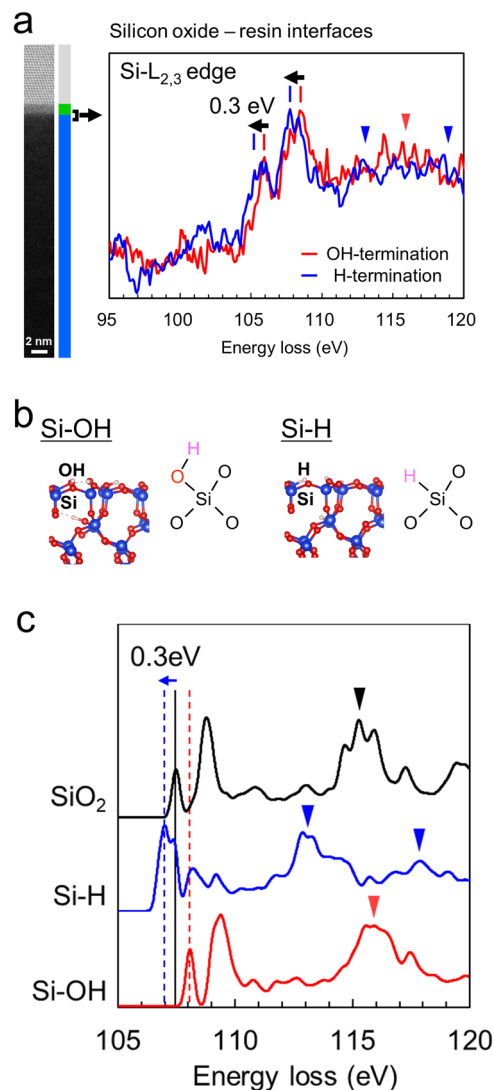


Fig. 3 | $\text{Si-L}_{2,3}$ edge electron energy-loss near-edge structure (ELNES) spectra of SiO_2 surfaces. a Experimental $\text{Si-L}_{2,3}$ edge spectra measured at the interfaces between the epoxy resin and OH- and H-terminated oxide layers with a width of 1 nm. **b** Surface models of OH- and H-terminated (0001) surfaces of α -quartz used for simulating $\text{Si-L}_{2,3}$ edge spectra. **c** Simulated $\text{Si-L}_{2,3}$ edge spectra from the Si atoms at the outermost surface of the models.

SiO_2 (Fig. 3a). Moreover, the chemical shift towards the lower-energy side in the experimental spectrum suggests the presence of numerous Si-H bonds that remain at the H-terminated interface, even after being covered with epoxy resin. Furthermore, in the spectrum of the H-terminated interface, the peak at 115 eV was not clearly observed, while additional peaks are observed at 112 and 118 eV. This change in the peak positions suggests that the Si atoms at the H-terminated interface exhibit distinct environments compared to the SiO_4 tetrahedral arrangement.

To explore other potential chemical bonds at the interfaces between the SiO_2 layer and the epoxy resin (DGEBA-PACM system), additional surface models were prepared, incorporating Si-O-phenyl, Si-O-C, Si-N, and Si-C bonds (Supplementary Fig. 6). Subsequently, $\text{Si-L}_{2,3}$ edge ELNES simulations were conducted based on these models. As illustrated in Supplementary Fig. 7, only the spectrum of the Si-C bond displays a chemical shift towards the lower-energy side when compared to the unmodified SiO_2 . Previous reports suggest that Si-H bonds can react with epoxy groups (albeit under UV irradiation), indicating the likelihood of Si-H bonds reacting with DGEBA molecules

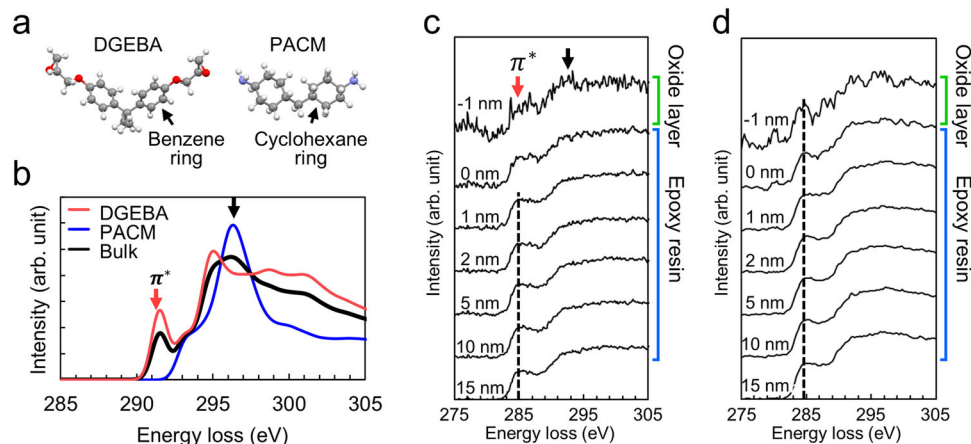


Fig. 4 | C-K edge spectra of the epoxy resin in the DGEBA-PACM system.

a Molecular structures of DGEBA and PACM used for the electron ELNES simulation. **b** Simulated C-K edge spectra for DGEBA, PACM, and the bulk of the epoxy resin (stoichiometric ratio of 1:1). The energy loss of the simulated spectra is not directly

compared to that of the experimental spectra. Experimental C-K edge spectra measured at various positions near the **c** OH-terminated and **d** H-terminated interfaces in 1 nm steps. The measured positions are indicated relative to the interface.

at the H-terminated interface. However, in such instances, a stable structure is formed by creating Si-O-C bonds rather than Si-C bonds²³. Consequently, the observed chemical shift in the Si-L_{2,3} edge spectrum towards the lower-energy side originates from the presence of Si-H bonds (H termination).

Compositional heterogeneity near the interfaces

The compositional ratio of DGEBA to PACM near the OH- and H-terminated interfaces was investigated using STEM-EELS (Supplementary Fig. 10). As depicted in Fig. 4a, b, the presence of aromatic rings (benzene rings) in the DGEBA molecular structure results in the appearance of a π^* peak at the C-K edge in the EEL spectrum. The π^* peak originates from the electron transition from the 1s to the π^* orbitals in C atoms. In contrast, the spectrum of PACM, without π bonds in its molecular structure, does not exhibit π^* peaks at the C-K edge. These distinct characteristics facilitated the identification of compositional heterogeneity within the epoxy resin. Furthermore, the energy loss in the simulated spectra differs from that observed in the experimental spectra by ~ 6 eV, attributed to calculation errors.

Figure 4c, d present the C-K edge spectra measured near the OH- and H-terminated interfaces, respectively. At every measured position, an π^* peak at 285 eV and a shoulder-like σ^* structure at 292 eV (representing the transition from 1s to σ^* orbitals) were observed. In the case of the OH-terminated interface, a decrease in the intensity of the π^* peak (red arrow) was observed around the surface of the oxide layer (-1 – 0 nm from the interface) compared to the bulk region of the epoxy resin (1 – 15 nm from the interface). This decrease in intensity signifies an increased ratio of PACM to DGEBA at the OH-terminated interface. Furthermore, the increased intensity at 292 eV (black arrow) supports the condensation of PACM at the OH-terminated interface. In contrast, the C-K edge spectra at the H-terminated interface exhibits a clear π^* peak with comparable intensity to that observed in the bulk region, suggesting minimal compositional changes at the H-terminated interface.

The profiles of the stoichiometric ratio (amine-to-epoxy ratio) were evaluated by dividing the π^* peak intensity by the σ^* peak intensity in the C-K edge spectrum, as described in Supplementary Note 10 in the Supplementary Information. These profiles in Fig. 5 (red circles) show that the stoichiometric ratio at the OH-terminated interface (~ 1.3) is larger than that in the bulk (1.0). In contrast, the epoxy resin close to the H-terminated interface shows a stoichiometric ratio of ~ 0.7 , which is smaller than that of the bulk region.

To verify the stoichiometry changes near the interfaces, compositional analysis of the epoxy resin was conducted using N-K-edge ELNES of the OH- and H-terminated interfaces. Since only PACM contains N atoms, the N-K edge spectra were attributed to PACM molecules. These spectra are presented in Supplementary Fig. 8. Although the N-K edge spectra exhibit weak signal intensities, making it challenging to analyse their spectral features, the relative amount of N atoms (representative of PACM) near the interfaces was determined by integrating the intensity of each N-K edge spectrum within the energy range of 400 – 420 eV. Furthermore, the integrated intensities of the C-K edge spectra within the range of 280 – 300 eV are approximately proportional to the quantity of all molecules, including DGEBA and PACM. Therefore, the integrated N-K edge intensity was normalized by the corresponding integrated C-K edge intensity, referred to as the “N-K/C-K intensity,” to estimate the relative ratio of PACM at each position from the interfaces. The blue squares in Fig. 5a, b depict the stoichiometric ratios calculated from the N-K/C-K intensities plotted against the distance from the OH- and H-terminated interfaces, respectively. In the case of the OH-terminated interface, the stoichiometric ratio of PACM is higher near the oxide-layer interface compared to the bulk region of the epoxy resin. Conversely, a gradual decrease in the stoichiometric ratio is observed for the H-terminated interface from the bulk toward interfacial regions. These profiles are consistent with those obtained from the C-K edge analysis.

The attenuated total reflection-Fourier transform infrared spectroscopy (ATR-FTIR) spectrum of the OH-terminated interface shows a higher peak intensity for the CH₂ vibrations compared to the H-terminated surface (Supplementary Fig. 4), supporting the observed condensation of PACM in that region. This is consistent with the higher amount of CH₂ groups in PACM compared to DGEBA, as discussed in Supplementary Note 6 of the Supplementary Information. Furthermore, the detection of PACM condensation by ATR-FTIR suggests that it is a prevalent feature across the entire OH-terminated interface.

Curing simulation of bulk systems of epoxy resins

The variations in the stoichiometric ratios of DGEBA to PACM should result in different cross-linked structures. To evaluate the cross-linked structures of the epoxy resin near the interfaces, we conducted curing MD simulations that consider the formation of cross-linked structures through exothermal reactions²⁴. Fig. 6a shows an example of a periodic cell model used to investigate the cross-linked structures formed in bulk systems with different stoichiometric ratios. The simulation considered the primary and secondary amine-epoxy reactions

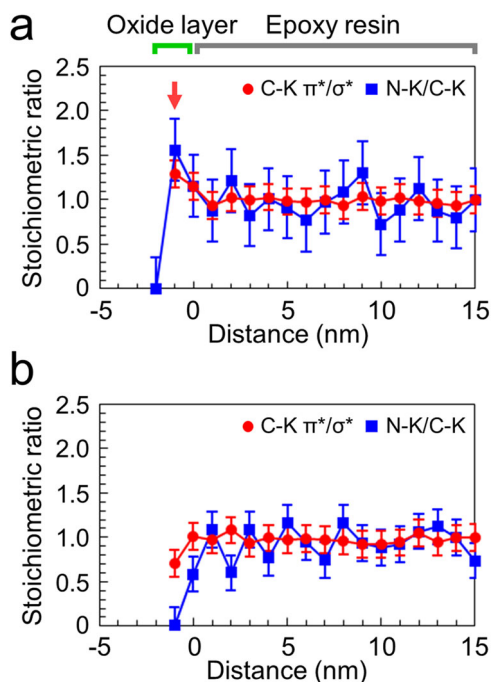


Fig. 5 | Profiles of the stoichiometric ratio (amine-to-epoxy ratio) measured at different distances from the adhesive interfaces. a OH-terminated and **b** H-terminated interfaces. The red circles represent the stoichiometric ratio estimated from the intensity of the π^* peak divided by that of the corresponding σ^* peak of the C-K edge spectrum (C-K π^*/σ^*). The blue squares indicate the stoichiometric ratio estimated from the integrated intensity of the N-K edge spectrum divided by that of the corresponding C-K edge spectrum (N-K/C-K). The error bars for the profiles estimated from the C-K π^*/σ^* intensities were defined as the errors of the curve fitting to the C-K edge spectra. The error bars for the profiles estimated from the N-K/C-K intensities were defined as the deviations from the average values in the regions within 5–15 nm from the interface, assuming that the stoichiometric ratio would be uniform in the region.

(Supplementary Fig. 5), forming linear secondary and branched tertiary amines and hydroxyl groups (Fig. 6b). Figure 6c shows that the number density of the tertiary amines (branched structures) is almost independent of the stoichiometric ratio, while those of the secondary amines (linear structures) and hydroxyl groups increase with increasing stoichiometric ratio.

Curing simulation on epoxy resin-silica interfaces

Subsequently, curing MD simulations of interfacial models were performed to explore the cross-linked and adhesion structures close to the OH- and H-terminated interfaces in detail. In the simulation, the (10 $\bar{1}$ 0) surfaces of α -quartz were terminated with OH and H as models of the oxidized Si layers, as shown in Fig. 7a. The uncured epoxy resin, consisting of DGEBA and PACM molecules, was confined between the OH- and H-terminated surfaces. The average stoichiometric ratios of the uncured epoxy resins within the OH- and H-terminated systems were set to reflect the interfacial compositions measured by STEM-EELS. Then, curing MD simulations were performed on these systems. Note that the simulations did not consider chemical reactions between the epoxy resin molecules and the substrates.

The stoichiometric ratios of the cured epoxy resins within 1 nm of the OH- and H-terminated interfaces (grey region in Supplementary Fig. 11) are -1.5 and 1.0, respectively, which are similar to the experimentally measured ratios. Figure 7b depicts the number density distributions of the reacted amino groups (secondary and tertiary amines) in the epoxy resins near the OH- and H-terminated interfaces. Within 1 nm of the interface (grey regions), the number densities of

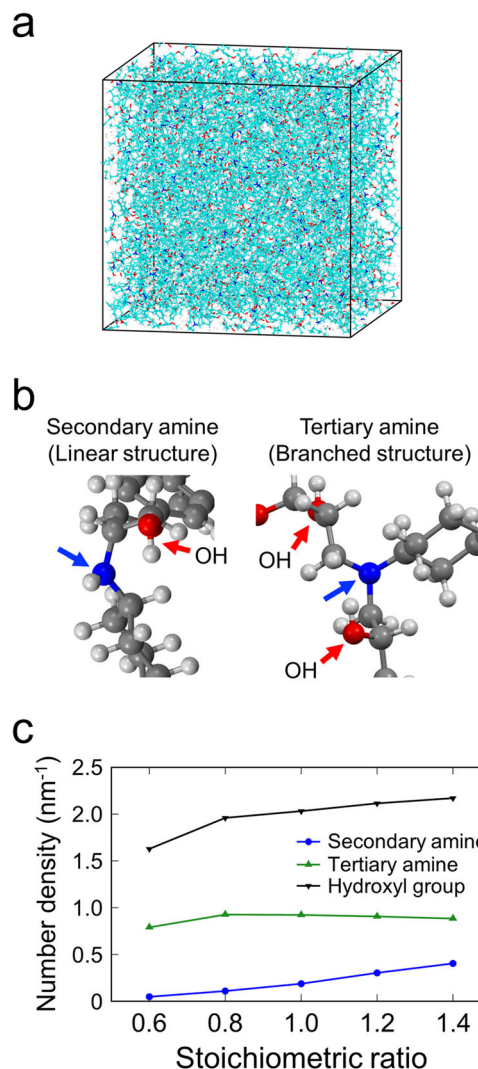


Fig. 6 | Curing molecular dynamic simulations of bulk systems of DGEBA-PACM epoxy resins with various stoichiometric ratios. a Model of the bulk system used for the simulations. **b** Schematics of the secondary and tertiary amine structures. Hydroxyl groups are generated by the reactions to form secondary and tertiary amines. **c** Number densities of the secondary and tertiary amines and hydroxyl groups as a function of the stoichiometric ratio.

tertiary amines (branched structures) are almost equal for both the OH- and H-terminated interfaces, whereas the OH-terminated interface, with a higher stoichiometric ratio, has more secondary amines (linear structures) than the H-terminated interface. This tendency is in good agreement with that of bulk systems, as shown in Fig. 6c. In other words, the OH-terminated interface has a higher average molecular weight between the cross-links than the H-terminated interface. The presence of distinct cross-linked structures at the interfaces could result in different mechanical properties²⁵.

The red lines in Fig. 7b show the distributions of the hydroxyl groups, originating from the reactions between epoxy and amino groups, as shown in Supplementary Fig. 5. The OH-terminated system exhibits a higher average density of the hydroxyl groups in the epoxy resin compared to the H-terminated system. This originates from the higher stoichiometric ratio in the OH-terminated system, as observed for the bulk system (Fig. 6c). Furthermore, the adsorption layers of hydroxyl groups exhibit a higher density near the OH-terminated interface compared to that near the H-terminated interface (denoted by black triangles). This difference arises from the formation of

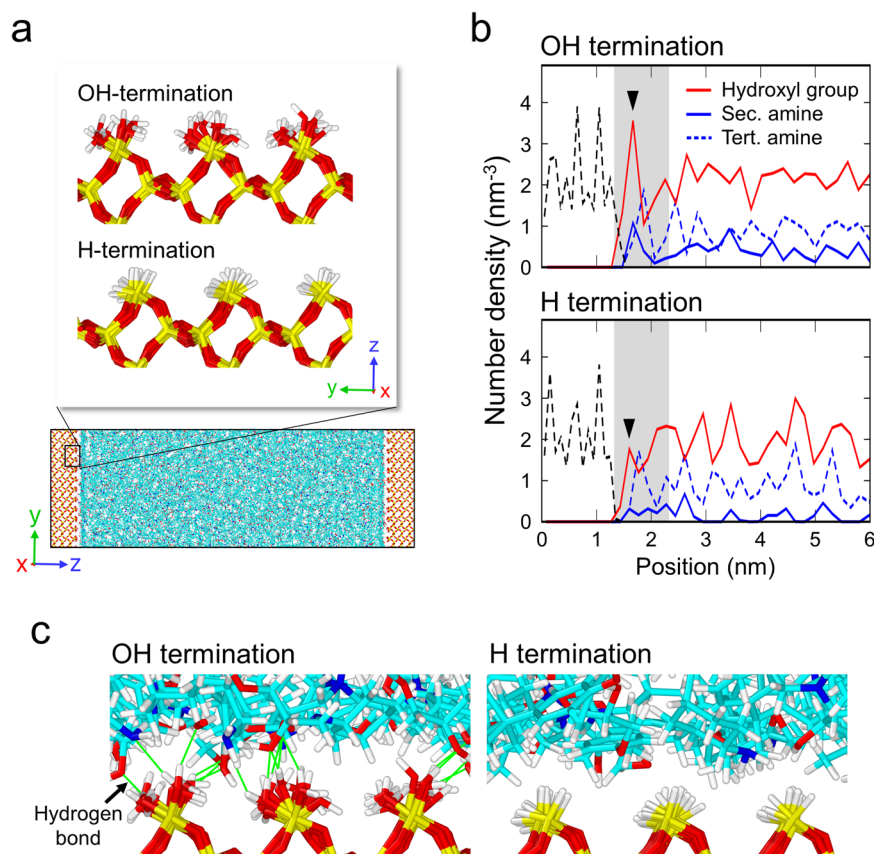


Fig. 7 | Epoxy resin structures cured at the OH- and H-terminated interfaces. **a** Simulation model before curing and the surface structures of the OH- and H-terminated SiO₂ (α -quartz) used for the curing molecular dynamics simulations. The top faces of the SiO₂ crystals are terminated with hydroxyl groups and hydrogen atoms, respectively. **b** Number densities of the secondary and tertiary

amines and hydroxyl groups in the epoxy resins near the OH- and H-terminated interfaces. The number densities of Si and O atoms in the substrates are shown by black dotted lines to clarify the positions of the interfaces. The regions within 1 nm of the interfaces are represented by grey. **c** Schematics of the OH- and H-terminated interfaces.

hydrogen bonds between the hydroxyl groups on the silica surface (silanol groups) and the hydroxyl groups generated within the epoxy resin.

Figure 7c illustrates the simulated atomic structure of the OH- and H-terminated interfaces. The hydrogen bonds (hydrogen-oxygen distance: <0.25 nm) between the silanol groups of the substrate and hydroxyl groups of the epoxy resin are indicated by green lines. The illustration indicates that numerous hydrogen bonds are formed at the OH-terminated interface, while there are very few hydrogen bonds at the H-terminated interface. Consequently, the OH-terminated interface with a PACM-rich composition generates many hydroxyl groups in the epoxy resin and preferentially forms hydrogen bonds to stabilize the adsorption structure.

The cross-linked structures exhibit stronger adhesion to the OH-terminated surfaces compared to the H-terminated surfaces due to hydrogen bonding. To quantitatively analyse the different interactions at the OH- and H-terminated interfaces, the adhesion energies of the epoxy resins on these surfaces were evaluated. The adhesion energy (E_{ad}) between the epoxy resin and the surfaces is defined as follows²⁶.

$$E_{ad} = (E_{epo} + E_{sub}) - E_{epo-sub} \quad (1)$$

Here, $E_{epo-sub}$ is the total energy of the interfacial model, and $(E_{epo} + E_{sub})$ is the total energy when the epoxy resin and SiO₂ substrates are separated. The adhesion strength is quantified by the magnitude of E_{ad} , where a higher value indicates stronger adhesion.

The E_{ad} values estimated for the OH- and H-terminated interfaces from the curing MD simulations were 0.223 and 0.147 J m⁻²,

respectively. These values indicate that the OH-terminated interface is energetically more stable and exhibits stronger surface adsorption. Although the magnitude of E_{ad} depends on the potential parameters utilized in the curing MD simulation, the relationship between the E_{ad} values of the OH- and H-terminated interfaces is consistent. These findings are supported by the contact angle analysis (Supplementary Note 3 and Supplementary Fig. 2). The contact angles of DGEBA, PACM, and the DGEBA-PACM mixtures on the OH-terminated surface are smaller than those on the H-terminated surface. This suggests that the OH-terminated surface energetically stabilizes both DGEBA and PACM molecules to a greater extent than the H-terminated surface, resulting in stronger molecular adsorption on the OH-terminated surface. The higher E_{ad} at the OH-terminated interface indicated by the MD simulation and contact-angle results is consistent with the results of a lap-shear test (Supplementary Fig. 12), where the OH-terminated interface demonstrated a stronger adhesive strength than the H-terminated interface. Consequently, the differences in cross-linked structures and E_{ad} at the OH- and H-terminated interfaces, which are dependent on the surface chemistry, are likely to influence the mechanical properties near the interfaces, particularly the fracture behaviour.

Fracture surfaces observed by TEM

To elucidate the fracture mechanisms near the OH- and H-terminated interfaces, cross-sectional TEM observations of fracture surfaces were conducted. Cross-sectional TEM specimens of the OH- and H-terminated interfaces, with a thickness of ~ 300 nm, were prepared using a focused ion beam (FIB). Subsequently, tensile loads were

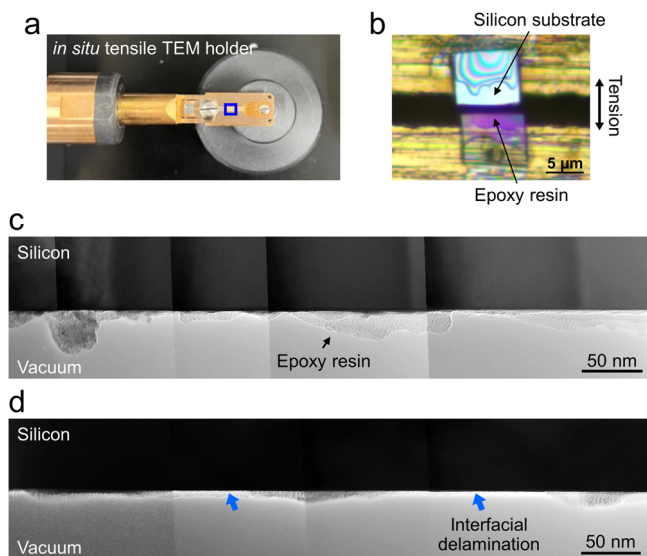


Fig. 8 | Transmission electron microscopy (TEM) observation of the fracture surfaces near the OH- and H-terminated interfaces. **a** Photograph of the tensile specimen holder with a tensile cartridge. **b** Magnified image of the region highlighted by the blue square in (a), showing an interface specimen bridged over the slit of the tensile cartridge. A tensile stress was applied to the interface between the epoxy resin and Si substrate to induce fracture as the slit was opened. Cross-sectional TEM images of the fracture surfaces near the (c) OH-terminated and (d) H-terminated interfaces.

applied perpendicular to the interfaces using a tensile TEM holder to induce fracture, as depicted in Fig. 8a, b^{27–29}. Although the loading conditions applied to the specimens of the lap-shear test were different from those of the tensile fracture tests with the TEM holder, we presumed that the strength relationships between the OH- and H-terminated interfaces were similar for both tensile and shear deformation since interfaces with weaker bonds are more likely to break at lower loads.

Figure 8c, d present the fracture surfaces of the OH- and H-terminated interfaces, respectively. In these cross-sectional TEM images, residual epoxy resin is observed on the top surfaces of the Si substrates at both the OH- and H-terminated interfaces. The average thicknesses of the residual epoxy resin layers are -11 and -6 nm for the OH- and H-terminated interfaces, respectively. Additionally, while the fracture surface of the OH-terminated interface is entirely located within the epoxy region (cohesive failure), half of the fracture surface of the H-terminated interface is at the interface itself (interfacial delamination).

The distinct fracture surfaces and mechanisms near the OH- and H-terminated interfaces are attributed to differences in the surface chemistry, i.e., different cross-linked structures and E_{ad} values. As depicted in Fig. 9, the OH-terminated interface exhibits higher E_{ad} , leading to fractures occurring within the epoxy resin (cohesive failure) without interfacial delamination. The non-linear fracture path is attributed to the heterogeneity in the cross-linked structure of the epoxy resin³⁰. In contrast, the interfacial delamination of the H-terminated interface is attributed to the lower adhesion energy at the interface. However, residual epoxy resin was observed on the surface of the Si substrate. H termination on Si substrates has been reported to be replaced by OH termination over time when the material is exposed to air^{31,32}. In this case, the areas with OH termination would exhibit similar fracture behaviours to the OH-terminated interface, namely cohesive failure, even at the H-terminated interface.

The exclusive condensation of PACM at the OH-terminated interface indicates distinct cross-linked structures of the epoxy

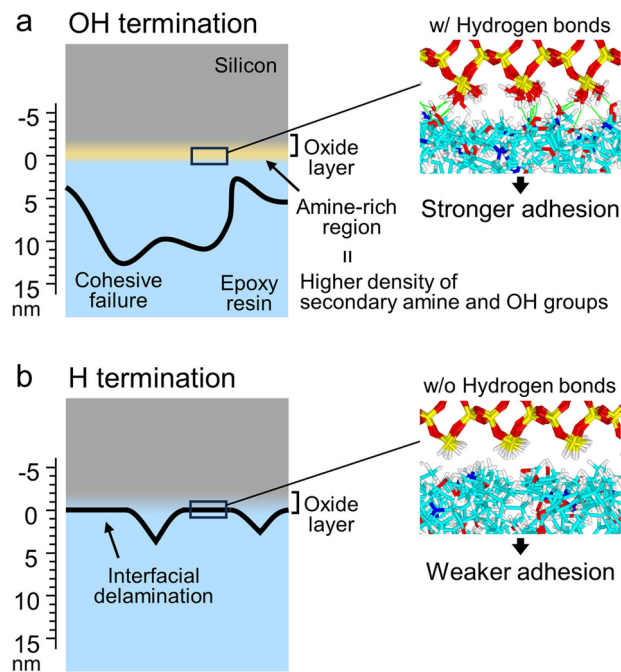


Fig. 9 | Schematics of the interfacial structures and fracture paths near the adhesive interfaces. (a) OH-terminated and (b) H-terminated interfaces.

resins near the OH- and H-terminated interfaces, even at the nanoscale. As cracks propagated within a single nanometre from the adhesive interfaces, the dissimilarity in the cross-linked structures of the epoxy resin near the interfaces influences the energy required for crack propagation. The distinct fracture mechanisms and cross-linked structures of the epoxy resins near the OH- and H-terminated interfaces led to different adhesive strengths, as measured by the lap shear test.

This study firstly examined the effects of the surface chemistry (OH and H termination) of Si substrates on the composition, cross-linked structure, and fracture mechanisms of epoxy resin near adhesive interfaces. Lap shear tests were conducted to quantify the adhesive strength, showing that the OH-terminated interface exhibited -13% higher adhesive strength than the H-terminated interface. To understand the underlying reasons for this discrepancy in adhesive strength, high-resolution TEM/STEM and curing MD simulations were employed for detailed analysis.

The Si-L_{2,3} edge ELNES spectra provided insights into the H termination remaining even after the resin was applied and cured on the surface. In contrast, the C-K and N-K edge ELNES spectra indicated that the PACM curing agent condensed (resulting in a higher stoichiometric ratio than that of the bulk) within a 1–2 nm range at the OH-terminated interface, whereas the opposite phenomenon was observed at the H-terminated interface (smaller stoichiometric ratio than that of the bulk). These findings were corroborated by ATR-FTIR measurements. The Si substrates have a sufficiently flat surface with a roughness of -0.5 nm, and the oxide layers have comparable thicknesses at both the OH- and H-terminated interfaces. Given these conditions, we conclude that the disparity in surface chemistry solely accounts for the variations in chemical composition near the interfaces.

Curing MD simulations further indicated that the compositional differences in the epoxy derived from the surface chemistry of the Si substrate influenced the cross-linked structures near the interfaces. Additionally, the adhesion energy at the OH-terminated interface was higher (indicating greater stability) than that of the H-terminated interface due to the adsorption of the epoxy resin on the OH-terminated surface via hydrogen bonds.

TEM observations of the fractured surfaces revealed distinct fracture behaviours between the OH-terminated surface and H-terminated interfaces. The OH-terminated interface exhibited cohesive failure due to its higher adhesion energy, while the H-terminated interface showed partial interfacial delamination due to its lower adhesion energy.

These findings clearly demonstrated the significant influence of the intermolecular interactions at adhesive interfaces the surface chemistry of inorganic substrates on both the molecular segregation and cross-linked structures of epoxy resin interfacial interactions between the epoxy resin and substrates and the epoxy resin cross-linked structures near the interfaces at a single-nanometre scale. The structural changes in the epoxy resin due to the surface chemistry near the interfaces are directly linked to have implications for the interfacial adhesive strengths and the propagation path of cracks near the interfaces. The acquired knowledge of the chemical interactions at the adhesive interfaces contributes to a comprehensive understanding of the interfacial adhesion and fracture mechanisms between polymers and inorganic materials.

Methods

Surface modification of Si substrates

Si single crystals with a surface orientation of (111) and a purity exceeding 99.999% were obtained from Crystal Base Co., Ltd., Japan. The Si substrates underwent surface modifications to create H- and OH-terminations through the following procedures. Initially, all organic residues on the Si surface were eliminated by immersing the Si substrate in a piranha solution (3:1 ratio of sulfuric acid to hydrogen peroxide). Subsequently, the hydroxyl groups on the Si surface were eliminated by immersing the Si substrate in a dilute solution of HF acid (1.5 wt.%) for 30 min to generate H-terminated Si surfaces. Additionally, some of the H-terminated surfaces underwent treatment with water vapour plasma for 20 min to introduce hydroxyl groups³³.

Measurement of contact angles on Si substrates

The contact angles of water, DGEBA (JER YL6810, Mitsubishi Chemical Corporation, purity: 100%), PACM (Tokyo Chemical Industry Co., Ltd., purity: >97.0%), and a DGEBA–PACM mixture with a stoichiometric ratio of 1:1 (pre-cured epoxy resin) on OH- and H-terminated Si substrates were measured. Water contact angles were measured at room temperature. In contrast, the contact angles of DGEBA, PACM, and the DGEBA–PACM mixture were measured at 60 °C (above the melting temperatures of DGEBA (40–44 °C) and the glass transition temperature of PACM (30–60 °C) determined by differential scanning calorimetry). The contact angle θ values of the droplets on the Si substrates were determined using the $\theta/2$ method and the following equation:

$$\theta = 2 \cdot \arctan\left(\frac{h}{r}\right) \quad (2)$$

Where h and r denote the height and radius of the droplet on the substrate, respectively.

Water contact angle, ATR-FTIR, and ellipsometry measurements were conducted within 30 min of the surface treatments, a timescale similar to that of the epoxy resin on Si substrates during the preparation of the interface specimens used for the interfacial analyses.

Preparation of epoxy resin–Si substrate interfaces

DGEBA and PACM were mixed in a stoichiometric ratio of 1:1, corresponding to a molar ratio of 2:1 for DGEBA to PACM. These reagents were mixed using the following process: (i) a vial bin containing DGEBA and PACM was heated at 60 °C, above the melting temperatures of DGEBA (40–44 °C) and the glass transition temperature of PACM (30–60 °C), for 5 min; (ii) the melting mixture was stirred for 5 min using a homogenizer (Power Homogenizer Portable S-203, AS ONE

Corporation, Japan) which produces many bubbles; (iii) vacuum degassing was performed using a rotary pump at room temperature until the bubbles were removed. To prepare the adhesive interfaces, a mixture of DGEBA and PACM was applied to the Si substrates and subsequently cured at 100 °C for 90 min. The thicknesses of the applied epoxy resin were 190 μm , 20 μm , 20 μm , and 1 mm for the lap-shear test pieces, STEM-EELS specimens, TEM specimens for fracture-surface observations, and ATR-FTIR specimens, respectively. Because these thicknesses are sufficiently larger than the regions where the compositional changes and fractures are observed (within ~ 10 nm of the interfaces with the silicon substrates), the phenomena occurring near the interfaces should be common for all specimens.

The degree of cross-linking of the epoxy resins was determined to be $\sim 85\%$ using ATR-FTIR. The changes in the peak intensity at 910 cm^{-1} (epoxy rings) during curing were standardized using the constant peak intensity at 830 cm^{-1} (benzene rings), which remained unchanged throughout the curing process.

FTIR measurement

Transmission FTIR and ATR-FTIR measurements were conducted using an FTIR Spectrometer Frontier (PerkinElmer, Inc., USA). The Si substrates used for ATR-FTIR analysis were obtained from R-DEC Co. To enable a fair comparison with the transmission FTIR spectra, the ATR-FTIR spectra were corrected by dividing them by the wavelength λ . This correction accounts for the fact that the absorbance in ATR-FTIR spectra is proportional to d_p ($\propto \lambda$), as shown in equation S2 of the Supplementary Information. The OH- and H-terminated Si substrates were coated with the epoxy resin and cured using the aforementioned conditions.

Lap shear tests

These tests were conducted to measure the adhesive strength between the epoxy resin and Si substrates. Two OH- and H-terminated Si substrates, each measuring 25 mm in width and 10 mm in length, were bonded to the DGEBA–PACM epoxy resin. A single-sided release film with a rectangular hole (25 mm width and 2 mm length) filled with a mixture of DGEBA and PACM was sandwiched between two Si substrates. The assembly was then heated at 100 °C for 90 min to cure the epoxy resin. The lapped region of the epoxy resin measured 25 mm in width, 2 mm in length, and 0.19 mm in thickness.

Furthermore, SUS304 plates measuring 25 mm in width, 100 mm in length, and 3 mm in thickness were bonded to both sides of the test pieces using a room-temperature curing adhesive. Small pieces consisting of two Si substrates, a release film, and a SUS plate were also attached to both ends of the SUS plates to adjust the thickness. The test pieces were mounted on a universal testing machine (Instron 5567, Instron Corporation, USA) with a 20 kN static load cell. The lap-shear tests were conducted at a tensile speed of 0.5 mm/min. The lap shear strength (adhesive strength) was calculated by dividing the load at the break by the lap area of 25 mm \times 2 mm.

STEM observation and STEM-EELS measurements

The ultrathin cross-sectional TEM specimens of the Si–epoxy interfaces were prepared by Ar ion milling at ~ -170 °C using a Cryo Ion Slicer IB-09060CIS (JEOL Ltd., Japan). STEM images and EELS spectra, specifically C–K, N–K, and O–K edge ELNES, were acquired using a STEM system (JEM-ARM200F, JEOL Ltd., Japan). The microscope was equipped with a cold field emission source, aberration correctors for the probe- and image-forming lenses, and an EELS system (Enfium ER, Gatan, Inc., USA) operated at 200 kV. The spectrometer was configured with a dispersion of 0.1 eV per channel, while the energy resolution of the EELS measurements was ~ 0.7 eV. Spectral imaging was conducted using a probe current of 30 pA, a probe size of ~ 0.1 nm, a dwell time of 4 s per pixel, a step size of 1 nm, and an image area of 5 pixels \times 20 pixels (corresponding to 5 nm \times 20 nm). A random sub-

pixel scan of 64 pixels was used to minimize electron irradiation damage. The irradiation damage had little impact on the major features of the C–K edge in the epoxy resin (DGEBA–PACM system) under the illumination condition. In particular, the peak intensities related to electron transitions from $1s$ to π^* and σ^* orbitals showed minimal changes³⁴. The spectra obtained from the pixels were integrated along the direction parallel to the interface to improve the signal-to-noise ratio.

Si- $L_{2,3}$ edge ELNES was measured from the interfaces between the epoxy resin and the SiO_2 layer using a STEM (JEM-ARM200F, JEOL Ltd., Japan). The microscope was equipped with a Schottky emission source, a double Wien filter monochromator, aberration correctors for the probe-forming and image-forming lenses, and a Quantum ERS EELS system (Gatan, Inc., USA). The measurements were conducted at an acceleration voltage of 200 kV. The spectrometer was set at a dispersion of 0.1 eV/channel, and the energy resolution of the EELS measurements was 0.3 eV. Spectral imaging was performed with a probe current of 3.7 pA, probe size of 0.1 nm, dwell time of 1.7 s/pixel, step size of 1 nm/pixel, and image area of 5 pixel \times 5 pixel (5 nm \times 5 nm). To minimize electron irradiation damage, a random sub-pixel scan of 64 pixels was applied.

Model preparation for ELNES simulations

To prepare stable structural models of SiO_2 surfaces with molecules, we performed structural optimization and molecular dynamics simulations based on density functional theory (DFT) calculations using Quantum Espresso software (ver. 6.4.1)³⁵. We prepared OH- and H-terminated surface models (Fig. 3) based on a stable 96-atom SiO_2 dense surface, corresponding to the 2×2 unit-cells of an α -quartz (0001) dense surface model^{36,37}. We applied the gauge-including-projector-augmented-wave method along with the Perdew–Burke–Ernzerhof exchange–correlation functional, specifically using pseudopotentials for {Si, O, and H}.pbe-tm-gipaw.UPF. To ensure accurate calculations, a k-point grid corresponding to the Brillouin zone gamma point was employed. For the plane-wave functions, a kinetic energy cut-off of 45.0 Ry was utilized, while a cut-off of 450.0 Ry was used for the charge density. To achieve stable structural models, we performed stabilization through a 500-fs run using DFT calculations at 300 K, consisting of 2000 MD steps with a time step of 0.25 fs.

To create grafted models of the H-terminated SiO_2 surface, we substituted the H atom with different molecules (-O-Ph, -O-C, -N, and -C), as depicted in Supplementary Fig. 6. Subsequently, structural optimizations and MD simulations were conducted using the same parameters and conditions as those applied to the OH-terminated and H-terminated surface models.

ELNES simulations

The C–K edge ELNES spectra were simulated using the first principles plane wave basis pseudopotential method (CASTEP code)³⁸ on structure-optimized DGEBA and PACM molecules in $1.5 \text{ nm} \times 1.5 \text{ nm} \times 1.0 \text{ nm}$ supercells. The structures used for the simulations are depicted in Fig. 4c. The C–K edges of all C sites within the models were individually calculated by incorporating the excited-state pseudopotential specific to each atomic site. The theoretical transition energies for all the spectra were determined using a method described in previous studies^{39,40}. The individual spectra within each model were combined to generate the overall spectrum of the model. A Gaussian distribution with a full width at half maximum of 0.5 eV was applied to broaden the spectra.

Si- $L_{2,3}$ edge ELNES simulations were conducted on epoxy resin–silica interface models to analyse the chemical bonding states at the interfaces between the epoxy resin and Si substrate. The Si- $L_{2,3}$ edge corresponds to the electron transition from the Si-2p orbital, which is a shallower state compared to the C-1s orbital used for C–K edges. To perform these simulations, a different simulation code

called the first-principles all-electron orthogonalized linear combination of atomic orbital code was employed⁴¹. For the Si- $L_{2,3}$ edge simulations, different functional groups (-H, -OH, -O-Ph, -O-C, -N, and -C) were attached to a Si atom on the α -quartz (0001) dense surface (as shown in Fig. 3 and Supplementary Fig. 6). A vacuum layer with a thickness of 1 nm was included in each model. The sizes of the models varied, ranging from $1 \times 1 \times 2\text{--}3 \text{ nm}$, depending on the size of the adsorbed species. To accurately distinguish the spectral differences between the surface models, the Si- $L_{2,3}$ edge spectra of the Si atoms bonded to the additional species (-H, -OH, -O-Ph, -O-C, -N, and -C) were simulated by introducing a core hole into the Si-2p orbital. The theoretical transition energy was estimated by calculating the total energy difference between the ground and excited states.

Curing molecular dynamics simulations

First, curing MD simulations for bulk systems without walls were performed to clarify the relationship between the stoichiometric ratios and cross-linked structures of the DGEBA–PACM epoxy resin system. To prepare the bulk systems with various stoichiometric ratios of 0.6, 0.8, 1.0, 1.2, and 1.4, the numbers of DGEBA and PACM molecules contained in the periodic cells were set to 420:126, 420:168, 420:210, 420:252, and 420:294, respectively. The DGEBA and PACM molecules were randomly packed in the cells with the procedure used in the previous studies^{42,43}.

Subsequently, curing MD simulations were conducted utilizing the reaction model proposed by Okabe et al.²⁴. The reaction criteria for the curing MD simulations were based on the distance between the reaction sites and the Arrhenius-type reaction probabilities calculated using activation energies and local temperatures. After the reaction, the heat of formation was released as kinetic energy at the reaction sites. Further details on the procedure for curing MD simulations can be found in previous reports^{24,42,43}. In this study, a distance criterion of 5.64 Å was used. The activation energy and heat of formation for the primary amine-epoxy reaction were 42.72 and 21.92 kcal mol⁻¹, respectively. For the secondary amine-epoxy reaction, the activation energy and heat of formation were 31.94 and 19.45 kcal mol⁻¹, respectively. The activation energies and heat of formation were computed using global reaction route mapping (GRRM)^{44–47} at the B3LYP/6-31 G(d) theoretical level. Annealing and cooling simulations were performed to prepare a cured resin model at room temperature^{25,48}. The DREIDING force fields were used for the polymers⁴⁹. Partial atomic charges were assigned using QEq^{50–52}. The parameters suggested by Lopes et al. were employed along with the CHARMM force field for the silica walls⁵³. All MD simulations were performed using LAMMPS⁵⁴.

Finally, curing MD simulations were conducted to investigate the behaviour of epoxy resins confined between silica walls with different surface chemistries. First, as depicted in Fig. 7a, the (10 $\bar{1}$ 0) surfaces of α -quartz SiO_2 were terminated with OH and H groups, representing the SiO_2 layers. These surfaces exhibit periodic structures in the x - and y -directions and a surface structure in the z -direction. Subsequently, a random arrangement of DGEBA and PACM molecules was introduced between the two silica surfaces. It is difficult to completely reproduce the species distribution inside the adhesive layer in a small system such as MD simulations. To reproduce the stoichiometric ratios near the interface obtained from EELS, curing MD simulations were performed by changing the overall stoichiometric ratio for the OH-terminated and H-terminated systems, respectively. For the OH-terminated system, the overall stoichiometric ratio was set to 1.4 using 720 DGEBA and 504 PACM molecules. For the H-terminated system, 720 DGEBA and 288 PACM molecules were used, and the stoichiometric ratio was set to 0.8. Initially, the cell dimensions were set to $58.9 \text{ Å} \times 63.6 \text{ Å} \times 851.5 \text{ Å}$, and the temperature was set to 327 °C. The MD cell was then compressed along the z -direction until the cell length reached 251.5 Å, while maintaining a constant temperature. Following compression, the system was cooled to the curing temperature of 100 °C under constant

volume conditions. Finally, an NPT simulation was performed for 2 ns at 100 °C and a pressure of 1 atm to allow for relaxation. The following curing simulations were conducted with the same conditions as those used for the bulk systems described above.

TEM observation of fracture surfaces

Thin cross-sectional sections of the OH- and H-terminated interfaces were obtained using a FIB system (JEM-9310FIB, JEOL Ltd., Japan). Each section had a thickness of ~300 nm. The sections were then mounted on tensile cartridges, positioned to bridge the slit (width of ~5 μm), ensuring that the interfaces were located inside the slit. The interfacial specimens were subjected to tensile loading and fracture at a rate of ~100 nm s⁻¹ using the tensile TEM holder. Following the fracturing process, the TEM holder was inserted into a TEM JEM-F200 (JEOL Ltd., Japan). Cross-sections of the fracture surfaces were observed using TEM.

Data availability

Source data of the ADF-STEM images are provided with this paper. The atomic coordinates of the cured bulk structures of epoxy resin with various stoichiometric ratios generated by the curing MD simulations are provided as Supplementary Data 1. The atomic coordinates of the OH- and H-terminated interfaces generated by the curing MD simulations are provided as Supplementary Data 2. Source data are provided with this paper.

References

- Petrie, E. M. *Handbook of Adhesives and Sealants* 2nd edn (McGraw-Hill Education, 2007).
- Wei, H. et al. Adhesion and cohesion of epoxy-based industrial composite coatings. *Compos. Part B Eng.* **193**, 108035 (2020).
- Jin, F., Li, X. & Park, S. Synthesis and application of epoxy resins: a review. *J. Ind. Eng. Chem.* **29**, 1–11 (2015).
- Sharpe, L. H. The interphase in adhesion. *J. Adhes.* **4**, 51–64 (1972).
- Swain, R. E., Reifsnider, K. L., Jayaraman, K. & El-Zein, M. Interface/interphase concepts in composite material systems. *J. Thermoplast. Compos. Mater.* **3**, 13–23 (1990).
- Horiuchi, S., Liu, Y., Shigemoto, Y., Hanada, T. & Shimamoto, K. In-situ TEM investigation of failure processes in metal-plastic joint interfaces. *Int. J. Adhes. Adhes.* <https://doi.org/10.1016/j.ijadhadh.2021.103003> (2021).
- Wang, P. et al. In situ transmission electron microscopy observation of the deformation and fracture processes of an epoxy/silica nanocomposite. *Soft Matter* **18**, 1149 (2022).
- BERG, J. C. Chapter 1 - Semi-empirical strategies for predicting adhesion. In (eds. Dillard, D. A., Pocius, A. V & Chaudhury, M. B. T.-A. S. and E.) 1–73 (Elsevier Science B.V., 2002).
- Drzal, L. T. In *Tough Composite Materials: Recent Developments* (eds. AG, E. & AE, Y.) 207 (Noyes Publication, 1985).
- Piggott, M. R. The effect of the interface/interphase on fiber composite properties. *Polym. Compos.* **8**, 291–297 (1987).
- Zhuravlev, L. T. The surface chemistry of amorphous silica zhuravlev model. *Colloids Surf. A Physicochem. Eng. Asp.* **173**, 1–38 (2000).
- Lenhart, J. L. & Wu, W. L. Deviations in the thermal properties of ultrathin polymer network films. *Macromolecules* **35**, 5145–5152 (2002).
- Chung, J., Munz, M. & Sturm, H. Stiffness variation in the interphase of amine-cured epoxy adjacent to copper microstructures. *Surf. Interface Anal.* **39**, 624–633 (2007).
- Aoki, M., Shundo, A., Okamoto, K., Ganbe, T. & Tanaka, K. Segregation of an amine component in a model epoxy resin at a copper interface. *Polym. J.* **51**, 359–363 (2019).
- Molitor, P., Barron, V. & Young, T. Surface treatment of titanium for adhesive bonding to polymer composites: a review. *Int. J. Adhes. Adhes.* **21**, 129–136 (2001).
- Park, S. Y., Choi, W. J., Choi, H. S., Kwon, H. & Kim, S. H. Recent trends in surface treatment technologies for airframe adhesive bonding processing: a review (1995–2008). *J. Adhes.* **86**, 192–221 (2010).
- Yamamoto, S., Kuwahara, R. & Tanaka, K. Effects of chemistry of silicon surfaces on the curing process and adhesive strength for epoxy resin. *ACS Appl. Polym. Mater.* **4**, 6038–6046 (2022).
- Horiuchi, S., Liu, Y., Hanada, T. & Akiyama, H. Applied surface science enhancement in adhesive bonding of aluminum alloy by steam treatment studied by energy loss near edge fine structures in electron energy loss spectroscopy. *Appl. Surf. Sci.* **599**, 153964 (2022).
- Garvie, L. A. J., Craven, A. J. & Brydson, R. Use of electron-energy loss near-edge fine structure in the study of minerals. *Am. Mineral.* **79**, 411–425 (1994).
- Tossell, J. A. The electronic structures of Mg, Al and Si in octahedral coordination with oxygen from SCF X α MO calculations. *J. Phys. Chem. Solids* **36**, 1273–1280 (1975).
- Garvie, L. A. J. & Buseck, P. R. Bonding in silicates: investigation of the Si L_{2,3} edge by parallel electron energy-loss spectroscopy. *Am. Mineral.* **84**, 946–964 (1999).
- Yoshiya, M., Adachi, H. & Tanaka, I. Interpretation of Si-L_{2,3} edge electron energy loss near edge structures (ELNES) from intergranular glassy film of Si₃N₄. *Ceram. J. Am. Ceram. Soc.* **82**, 3231–3236 (1999).
- Soliman, A. I. A., Utsunomiya, T., Ichii, T. & Sugimura, H. 1,2-Epoxyalkane: another precursor for fabricating alkoxy self-assembled monolayers on hydrogen-terminated Si(111). *Langmuir* **34**, 13162–13170 (2018).
- Okabe, T. et al. Curing reaction of epoxy resin composed of mixed base resin and curing agent: experiments and molecular simulation. *Polymer* **54**, 4660–4668 (2013).
- Odagiri, N. et al. Amine/epoxy stoichiometric ratio dependence of crosslinked structure and ductility in amine-cured epoxy thermosetting resins. *J. Appl. Polym. Sci.* **138**, 1–14 (2021).
- Nakamura, S., Yamamoto, S., Tsuji, Y., Tanaka, K. & Yoshizawa, K. Theoretical study on the contribution of interfacial functional groups to the adhesive interaction between epoxy resins and aluminum surfaces. *Langmuir* **38**, 6653–6664 (2022).
- Higuchi, T. et al. Development of a three-dimensional tomography holder for in situ tensile deformation for soft materials. *Microscopy* **67**, 296–300 (2018).
- Miyata, T. et al. Nanoscale stress distribution in silica-nanoparticle-filled rubber as observed by transmission electron microscopy: implications for tire application. *ACS Appl. Nano Mater.* **4**, 4452–4461 (2021).
- Shimizu, K., Miyata, T., Nagao, T., Kumagai, A. & Jinnai, H. Visualization of the tensile fracture behaviors at adhesive interfaces between brass and sulfur-containing rubber studied by transmission electron microscopy. *Polymer* **181**, 121789 (2019).
- Vidil, T., Tournilhac, F., Musso, S., Robisson, A. & Leibler, L. Control of reactions and network structures of epoxy thermosets. *Prog. Polym. Sci.* **62**, 126–179 (2016).
- Kolibal, M., Čechal, J., Bartošik, M., Mach, J. & Šikola, T. Stability of hydrogen-terminated vicinal Si(111) surface under ambient atmosphere. *Appl. Surf. Sci.* **256**, 3423–3426 (2010).
- Ogawa, H., Ishikawa, K., Inomata, C. & Fujimura, S. Initial stage of native oxide growth on hydrogen terminated silicon (111) surfaces. *J. Appl. Phys.* **79**, 472–477 (1996).
- Mizukami, M., Nakagawa, Y. & Kurihara, K. Surface induced hydrogen-bonded macrocluster formation of methanol on silica surfaces. *J. Am. Chem. Soc.* **124**, 12889–12897 (2002).

34. Yoshida, K., Huang, H.-H., Miyata, T., Sato, Y. K. & Jinnai, H. Electron irradiation damage of amorphous epoxy resin at low electron doses. *Microscopy* **72**, 361–367 (2023).
35. Giannozzi, P. et al. QUANTUM ESPRESSO: a modular and open-source software project for quantum simulations of materials. *J. Phys. Condens. Matter* **21**, 395502 (2009).
36. Rignanese, G., De Vita, A., Charlier, J., Gonze, X. & Car, R. First-principles molecular-dynamics study of the (0001) surface. *Phys. Rev. B - Condens. Matter Mater. Phys.* **61**, 13250–13255 (2000).
37. Hagita, K., Miyata, T. & Jinnai, H. Molecular dynamics simulations on epoxy/silica interfaces using stable atomic models of silica surfaces. *Langmuir* **39**, 7063–7078 (2023).
38. Clark, S., Segall, M. & Pickard, C. First principles methods using CASTEP. *Z. für Krist. - Cryst. Mater.* **220**, 567–570 (2005).
39. Mizoguchi, T. Overlap population diagram for ELNES and XANES: peak assignment and interpretation. *J. Phys. Condens. Matter* **21**, 104215 (2009).
40. Miyata, T. & Mizoguchi, T. Fabrication of thin TEM sample of ionic liquid for high-resolution ELNES measurements. *Ultramicroscopy* **178**, 81–87 (2017).
41. Ching, W. Y. Theoretical studies of the electronic properties of ceramic materials. *J. Am. Ceram. Soc.* **73**, 3135–3160 (1990).
42. Kawagoe, Y., Kikugawa, G., Shirasu, K. & Okabe, T. Thermoset resin curing simulation using quantum-chemical reaction path calculation and dissipative particle dynamics. *Soft Matter* **17**, 6707–6717 (2021).
43. Kawagoe, Y. et al. Multiscale modeling of process-induced residual deformation on carbon-fiber-reinforced plastic laminate from quantum calculation to laminate scale finite-element analysis. *Mech. Mater.* **170**, 104332 (2022).
44. Ohno, K. & Maeda, S. A scaled hypersphere search method for the topography of reaction pathways on the potential energy surface. *Chem. Phys. Lett.* **384**, 277–282 (2004).
45. Maeda, S. & Ohno, K. Global mapping of equilibrium and transition structures on potential energy surfaces by the scaled hypersphere search method: applications to ab initio surfaces of formaldehyde and propyne molecules. *J. Phys. Chem. A* **109**, 5742–5753 (2005).
46. Ohno, K. & Maeda, S. Automated exploration of reaction channels. *Phys. Scr.* **78**, 058122 (2008).
47. Maeda, S., Ohno, K. & Morokuma, K. Systematic exploration of the mechanism of chemical reactions: the global reaction route mapping (GRRM) strategy using the ADDF and AFIR methods. *Phys. Chem. Chem. Phys.* **15**, 3683–3701 (2013).
48. Kawagoe, Y., Surblyls, D., Matsubara, H., Kikugawa, G. & Ohara, T. Cross-plane and in-plane heat conductions in layer-by-layer membrane: molecular dynamics study. *Langmuir* **36**, 6482–6493 (2020).
49. Mayo, S. L., Olafson, B. D. & Goddard, W. A. DREIDING: a generic force field for molecular simulations. *J. Phys. Chem.* **94**, 8897–8909 (1990).
50. Rappé, A. K. & Goddard, W. A. Charge equilibration for molecular dynamics simulations. *J. Phys. Chem.* **95**, 3358–3363 (1991).
51. Zhang, L. et al. Carbon cluster formation during thermal decomposition of octahydro-1,3,5,7-tetranitro-1,3,5,7-tetrazocine and 1,3,5-triamino-2,4,6-trinitrobenzene high explosives from ReaxFF reactive molecular dynamics simulations. *J. Phys. Chem. A* **113**, 10619–10640 (2009).
52. Demir, B. & Walsh, T. R. A robust and reproducible procedure for cross-linking thermoset polymers using molecular simulation. *Soft Matter* **12**, 2453–2464 (2016).
53. Lopes, P. E. M., Murashov, V., Tazi, M., Demchuk, E. & MacKerell, A. D. Development of an empirical force field for silica. Application to the quartz-water interface. *J. Phys. Chem. B* **110**, 2782–2792 (2006).
54. Plimpton, S. Fast parallel algorithms for short-range molecular dynamics. *J. Comput. Phys.* **117**, 1–19 (1995).

Acknowledgements

This work was supported by the Japan Science and Technology Agency (JST) CREST to H.J. (Grant Numbers JPMJCR1993 and JPMJCR19T4) and the Japan Society for the Promotion of Science (JSPS) KAKENHI (Grant Numbers 20K15330 and 23H02017 to T.M. and 22H00329 to H.J.). STEM observations and EELS measurements were performed at the Tohoku University Microstructural Characterization Platform and Kyoto University Microstructural Characterization Platform in the Nanotechnology Platform Project, sponsored by the Ministry of Education, Culture, Sports, Science, and Technology (MEXT), Japan. We would like to thank Editage (www.editage.com) for English language editing.

Author contributions

The manuscript was written through contributions of all authors. All authors approved the final version of the manuscript. T.Miy., Y.K.S., and H.J. wrote the manuscript; T.Miy. and H.J. coordinated the experiments; T.Miy., Y.K.S., S.K., and M.M. prepared the specimens; T.Miy., S.K., and K.S. performed the lap-shear test; T.Miy. and Y.K. performed the STEM-EELS analysis; H.F.W. and A.K. performed the TEM observation; Y.K. and T.O. did the curing MD simulation; K.H. and T.Miz. contributed the ELNES simulation; T.Miy., Y.K.S., and M.M. contributed the ellipsometry, contact angle measurements, and ATR-FTIR measurements; K.S. contributed the finite element analysis; K.Y. and H.-H.H. helped interpret the results; H.J. supervised the project.

Competing interests

The authors declare no competing interests.

Additional information

Supplementary information The online version contains supplementary material available at <https://doi.org/10.1038/s41467-024-46138-6>.

Correspondence and requests for materials should be addressed to Yoshiaki Kawagoe, Keiichi Shirasu or Hiroshi Jinnai.

Peer review information *Nature Communications* thanks Suzanne Morsch and the other, anonymous, reviewers for their contribution to the peer review of this work. A peer review file is available.

Reprints and permissions information is available at <http://www.nature.com/reprints>

Publisher's note Springer Nature remains neutral with regard to jurisdictional claims in published maps and institutional affiliations.

Open Access This article is licensed under a Creative Commons Attribution 4.0 International License, which permits use, sharing, adaptation, distribution and reproduction in any medium or format, as long as you give appropriate credit to the original author(s) and the source, provide a link to the Creative Commons licence, and indicate if changes were made. The images or other third party material in this article are included in the article's Creative Commons licence, unless indicated otherwise in a credit line to the material. If material is not included in the article's Creative Commons licence and your intended use is not permitted by statutory regulation or exceeds the permitted use, you will need to obtain permission directly from the copyright holder. To view a copy of this licence, visit <http://creativecommons.org/licenses/by/4.0/>.

© The Author(s) 2024

¹Institute of Multidisciplinary Research for Advanced Materials, Tohoku University, Sendai, Miyagi 980-8577, Japan. ²Department of Aerospace Engineering, Graduate School of Engineering, Tohoku University, 6-6-01 Aramaki Aza Aoba, Aoba-ku, Sendai, Miyagi 980-8579, Japan. ³Department of Finemechanics, Graduate School of Engineering, Tohoku University, 6-6-01 Aramaki Aza Aoba, Aoba-ku, Sendai, Miyagi 980-8579, Japan. ⁴Department of Chemical and Materials Engineering, National Central University, No. 300, Zhongda Rd., Zhongli Dist., Taoyuan City 320317, Taiwan. ⁵Department of Applied Chemistry, Graduate School of Engineering, Tohoku University, 6-6-07 Aramaki Aza Aoba, Aoba-ku, Sendai, Miyagi 980-8579, Japan. ⁶New Industry Creation Hatchery Center, Tohoku University, Sendai, Miyagi 980-0845, Japan. ⁷Nanostructures Research Laboratory, Japan Fine Ceramics Center, Nagoya, Aichi 456-8587, Japan. ⁸Research Center for Structural Materials, Polymer Matrix Hybrid Composite Materials Group, National Institute for Materials Science, 1-2-1 Sengen, Tsukuba, Ibaraki 305-0047, Japan. ⁹Department of Materials Science and Engineering, University of Washington, BOX 352120, Seattle, WA 98195, USA. ¹⁰Department of Applied Physics, National Defense Academy, Yokosuka, Kanagawa 239-0811, Japan. ¹¹Institute of Industrial Science, The University of Tokyo, Meguro-ku, Tokyo 153-8505, Japan. ✉ e-mail: kawagoe@tohoku.ac.jp; keiichi.shirasu.c1@tohoku.ac.jp; hiroshi.jinnai.d4@tohoku.ac.jp